

Semi-visible jets + X: Illuminating Dark Showers with Radiation

Bingxuan Liu^a Kevin Pedro^b

^a*School of Science, Sun Yat-sen University, Shenzhen Campus, 66 Gongchang Road, Shenzhen, Guangdong 518107, PRC*

^b*Fermi National Accelerator Laboratory, Batavia, IL 60510, USA*

E-mail: liubx28@mail.sysu.edu.cn, pedrok@fnal.gov

ABSTRACT: We investigate the potential to search for semi-visible jets (SVJs) at the Large Hadron Collider (LHC) using initial-state radiation (ISR). Both photon ISR and jet ISR channels are considered, using a benchmark signal model with the decay of a leptophobic Z' mediator forming two SVJs. We compare and extend several techniques to decompose the missing transverse momentum into per-jet contributions, in order to reconstruct the mediator mass and to define a new observable measuring the fraction of invisible dark hadrons. The presence of ISR facilitates the identification of the SVJs, and the resulting boost improves the resolution of the observables, especially for models with high invisible fractions. We combine the two observables to propose a complete search strategy and discuss an extension of the strategy to probe the whole model parameter space.

KEYWORDS: Dark QCD, Dark Matter, New Physics, Semi-visible Jets, Large Hadron Collider

Contents

1	Introduction	2
2	Simulated Event Samples	4
3	Kinematic Properties	5
4	Analysis Strategy	11
5	Sensitivity Estimation	15
6	Outlook	18
A	Impacts of the Jet Clustering Radius	19
	References	21

1 Introduction

Although the standard model (SM) of particle physics has been proven to be a very successful theory whose theoretical predictions agree well with most experimental results, it does not explain all phenomena, such as the origin of dark matter (DM) [1–5]. Searching for DM has been one of the most critical tasks in particle physics. The Large Hadron Collider (LHC) is the only particle collider in the world that can reach a center-of-mass energy of 13.6 TeV, which offers a unique opportunity to search for a wide range of potentially accessible DM candidates. The LHC experiments, such as the CMS and ATLAS collaborations, have diverse DM search programs. Until very recently, they have been focused on models with weakly interacting massive particles (WIMPs) [6], where the DM candidates do not leave any trace in the detector, resulting in an imbalanced distribution of transverse momentum. Therefore, these classic DM searches consider events with large missing transverse momentum (E_T^{miss} , the magnitude of the two-vector \vec{p}_T^{miss}), and are categorized by the types of visible particles that recoil against the DM candidates. A large variety of scenarios have been explored, such as DM candidates recoiling against a jet [7, 8], a top quark [9–11], a vector boson [12, 13], a photon [14], or a Higgs boson [15–17]. This type of search assumes the DM candidates are clearly separated from the objects they recoil against, so they explicitly require \vec{p}_T^{miss} not to overlap with those objects. As a consequence, the traditional search strategies have limited sensitivity to models without this feature.

Dark sectors containing a new confining force $SU(N)$, an analog to quantum chromodynamics (QCD) in the SM, are well motivated from both the theoretical and experimental perspectives. If the scale of the new confining force, referred to as the dark QCD [18], is related to SM QCD, the models are consistent with the DM relic density [19]. Unlike the WIMP models where the DM candidates are produced directly, here the DM candidates are generated during the dark showering. The dark sector contains several flavors of dark quarks (χ_i), which form bound states called dark hadrons that may be either stable or unstable. The stable dark hadrons are DM candidates that will escape detection, while the unstable dark hadrons will decay promptly to SM particles. The mixture of visible and invisible decay products creates a striking feature called a “semi-visible” jet (SVJ) [20, 21]. The previous DM search program at the LHC is not optimal for such signatures, because of the required separation of \vec{p}_T^{miss} from visible objects mentioned above, as discussed in Refs. [22, 23].

SVJs are attracting more attention in the LHC physics program. CMS performed the first search for SVJs [22], which considers a heavy mediator, Z' , produced via a s -channel resonant production and decaying to dark quarks. A recent ATLAS analysis probes non-resonant production of SVJs [23]. The community has also identified a set of common model parameters in order to be able to compare results across experiments [24]. One model parameter, r_{inv} , which is the fraction of dark hadrons that are stable and invisible ($N_{\text{stable}}/(N_{\text{stable}} + N_{\text{unstable}})$), governs the experimental signatures. When r_{inv} approaches zero, the signal jets are fully visible rather than semi-visible. But they are still different from those jets expected in SM, as the complicated dark showering leads to changes in jet

substructure. ATLAS has published a result searching for such dark jets [25]. The typical dijet searches [26] have also explored a large phase space relevant to this scenario. If r_{inv} goes to one, the jets become fully invisible, so traditional DM searches relying on $E_{\text{T}}^{\text{miss}}$ become sensitive. CMS has recently demonstrated the complementary sensitivity of these strategies [27]. So far, the dedicated SVJ search strategies only cover a portion of the overall phase space for intermediate r_{inv} values.

The ATLAS and CMS searches for SVJs require either $E_{\text{T}}^{\text{miss}}$ or transverse momentum sum triggers. For possible signal processes, the former would exploit the missing energy from the invisible particles from the dark shower, while the latter would rely on the high momentum of the visible decay products. Consequently, it is challenging to optimize the search strategy for the entire range of r_{inv} values. In addition, the trigger thresholds are too high to include lower mediator masses. One common strategy adopted in dijet resonance searches to overcome this is to trigger on the initial state radiation (ISR). Though processes with substantial ISR have significantly reduced cross sections, this technique has been demonstrated to be sensitive to mediator masses from 700 down to 200 GeV [28, 29]. The ISR production channel has not yet been explored in the context of dark QCD searches. In this work, we show that it is a promising avenue. The unique features of SVJs also allow us to construct more powerful discriminating variables when the SVJ system is boosted against the energetic ISR. Depending on the mediator mass and the ISR momentum, the two SVJs can either be merged into one large-radius jet, or reconstructed as two separate small-radius jets. In this paper, we consider the latter case.

The benchmark signal process is the s -channel production of a new heavy particle (Z') that subsequently decays to two dark quarks [20, 21]. Figure 1 summarizes the leading-order production diagrams. We consider the scenarios where the ISR object is a jet or a photon, leaving other possibilities, such as a vector boson, to future work.

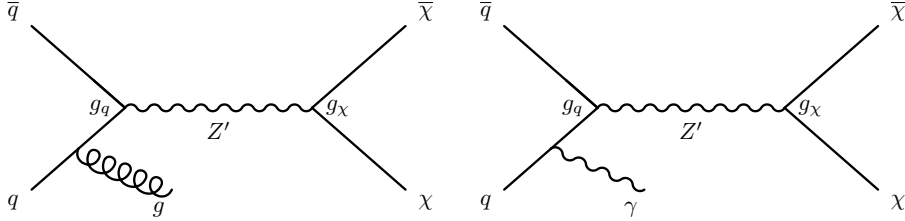


Figure 1: Feynman diagrams of the two Z' production channels considered in this work: Z' production in association with an ISR gluon (left) and Z' production in association with an ISR photon (right).

The article is organized as follows: Section 2 details the simulation procedure; Section 3 discusses the kinematic properties of the signal and background processes; Section 4 lays out a simple search strategy, followed by a summary of the sensitivity in Section 5; and finally, Section 6 gives an outlook and offers some further thoughts.

2 Simulated Event Samples

All samples used in this work are produced using MADGRAPH5_aMC@NLO 3.5.1 [30] for generation, PYTHIA 8.306 [31] for showering, and DELPHES 3.5.0 [32] for reconstruction. The CMS detector geometry and performance are used for reconstruction.

2.1 Signal Process

The signal grid is defined by the Z' mass and r_{inv} . Two mass points, 0.5 TeV and 1.0 TeV, are included to cover the most relevant kinematic region. Three r_{inv} values, 0.1, 0.5, and 0.9, span the whole r_{inv} range. Two additional mass points, 0.75 TeV and 1.25 TeV, with r_{inv} set to 0.9, are also generated to evaluate the sensitivity in Section 5. Since the only change for different r_{inv} values occurs during the showering step, the same generated events are reused. The CKKW-L scheme [33] is used to perform matrix element merging in PYTHIA 8.306, with a merging scale of 45. The details of the signal model follow Ref. [22], using the MADGRAPH implementation from Ref. [21]. Important parameters include g_q , the coupling between Z' and SM quarks, which is set to 0.25 for all quark flavors, and g_χ , the coupling between Z' and the dark quarks, which is set to $1/\sqrt{N_c^{\text{dark}} N_f^{\text{dark}}} = 0.5$. The latter takes into account N_c^{dark} , the number of dark colors, and N_f^{dark} , the number of dark flavors, which are both set to 2 in this model. The resulting branching fraction for $Z' \rightarrow \chi\bar{\chi}$, $\mathcal{B}(Z' \rightarrow \chi\bar{\chi})$, is therefore 47%, in agreement with the benchmark for simplified DM models [34]. The dark hadron masses are set to 20 GeV.

Handling the signal processes with an ISR photon is straightforward, as we do not expect energetic photons from Z' decays. The signal samples in this channel are generated with an additional photon. Processes with up to one additional parton besides the photon are included as well. The minimum p_T of the additional photon is set to 150 GeV in order to have appreciable acceptance from typical single photon triggers. Each signal sample contains 100,000 events.

The ISR jet channel is more complicated as there are also jets from Z' decays. Furthermore, the p_T of the jets from Z' decays depend on r_{inv} , which makes it necessary to generate the samples inclusively. Given that a typical single jet momentum trigger threshold approaches 500 GeV, the acceptance of the inclusive production mode is low. Therefore, each signal sample contains 500,000 events in the ISR jet channel. Up to two additional partons are included. Table 1 summarizes the processes generated in MADGRAPH5_aMC@NLO 3.5.1.

2.2 Background Process

The main background for this search comes from SM QCD multijet production. Two sets of samples are created. For the photon ISR channel, the sample includes multijet processes with one photon and up to three jets, where the photon is required to have p_T larger than 150 GeV. For the jet ISR channel, all multijet processes with up to four jets are included, where at least one jet has to pass $p_T > 500$ GeV. Each sample has 500,000 events produced. While applying selections at the generation level can introduce biases, the choices made here are sufficient for the scope of this study.

Table 1: The MADGRAPH processes used in the signal generation. The symbols x_d and $x_{d\sim}$ stand for dark quarks and dark antiquarks in this implementation, while j stands for an SM parton (quark or gluon).

Channel	Process	Generator Selection
ISR Photon	generate $p p \rightarrow x_d x_{d\sim} \gamma$ add process $p p \rightarrow x_d x_{d\sim} \gamma j$	$p_T^\gamma > 150 \text{ GeV}$
ISR Jet	generate $p p \rightarrow x_d x_{d\sim}$ add process $p p \rightarrow x_d x_{d\sim} j$ add process $p p \rightarrow x_d x_{d\sim} j j$	-

3 Kinematic Properties

This section discusses some interesting characteristics of the event kinematic properties for both the signal and background processes, in order to motivate the analysis strategy established in Section 4.

3.1 Basic Kinematics

Very loose fiducial selections are applied so that only events containing at least two jets with $p_T > 25 \text{ GeV}$ and $|\eta| < 4.5$ are considered. This is because of the proposed search strategy that relies on observables constructed using the two jets from the Z' and E_T^{miss} , as described in Section 4. The m_T is constructed using the two leading non-ISR jets and E_T^{miss} .

Some signal kinematic variables are strongly correlated with the p_T of the ISR object. Each signal jet originates from a dark quark that undergoes a showering process, producing a stochastic mixture of stable and unstable dark hadrons. If both jets have similar numbers of stable dark hadrons, the transverse component of the missing momentum will be symmetric between the jets and will mostly cancel, even for large r_{inv} . However, when there is an energetic ISR object recoiling against the Z' system, the resulting SVJs become more collimated. Events with either symmetric or asymmetric invisible components in the SVJs become more similar topologically, as illustrated in Figure 2.

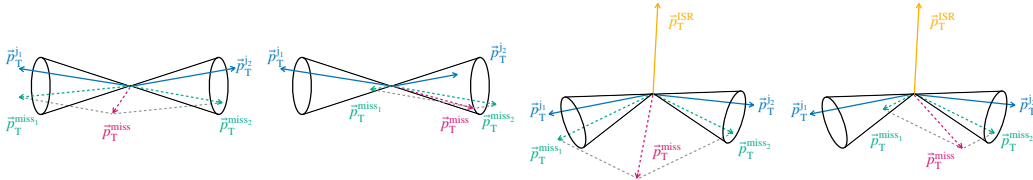


Figure 2: Diagrams illustrating the back-to-back topology and ISR topology, with symmetric and asymmetric invisible components in the SVJs.

Figure 3 shows that E_T^{miss} increases with r_{inv} when the p_T of the ISR object is high, while without an energetic ISR object, the E_T^{miss} depends less on r_{inv} , because of the cancellation of the symmetric invisible components. This enhancement of E_T^{miss} has remarkable impacts on the observables that will be discussed later. Another variable often used in heavy particle search is the rapidity difference y^* , defined as $(Y_1 - Y_2)/2$, where Y_i is the rapidity of a given jet [26]. In heavy particle decays, y^* for the two resulting jets has a smaller absolute value compared to the multijet background. This quantity is less affected than E_T^{miss} by the ISR object.

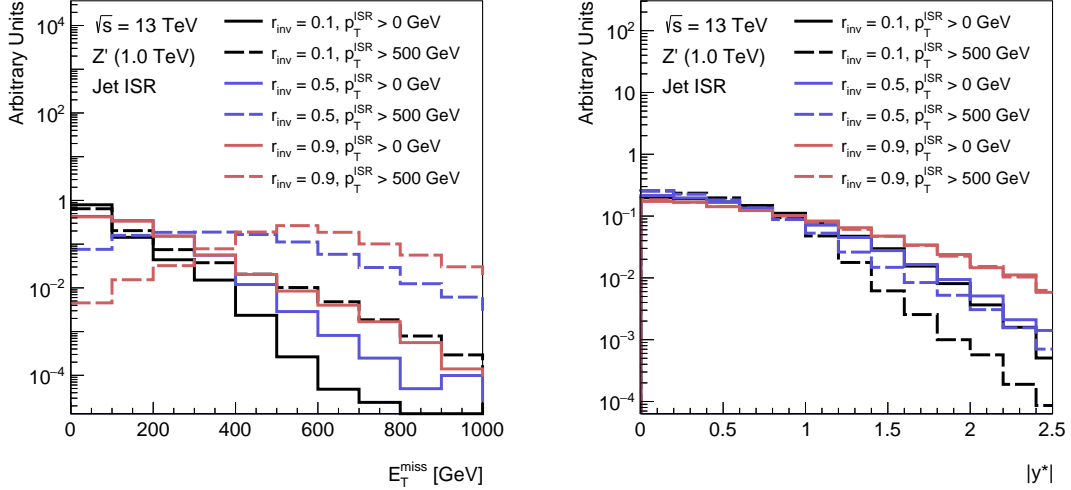


Figure 3: Left: E_T^{miss} distributions of the Z' samples for $m_{Z'} = 1.0$ TeV (right), with various r_{inv} and p_T^{ISR} . Right: $|y^*|$ distributions of the Z' samples for $m_{Z'} = 1.0$ TeV (right), with various r_{inv} and p_T^{ISR} .

The kinematic distributions of the multijet background process are also affected by the ISR object, as seen in Figure 4. The E_T^{miss} increases moderately as the p_T of the ISR object goes from 0 to 500 GeV, because there is no genuine source of sizable E_T^{miss} in the multijet process. The main source of E_T^{miss} in multijet events comes from jet misreconstruction caused by detector inefficiency and noise, such as inactive calorimeter cells and beam remnants. By construction, E_T^{miss} is balanced against the other visible objects, so when there exists an energetic ISR object, E_T^{miss} increases correspondingly. The increase is smooth, so in the next section, we will see it does not introduce discontinuities in the main observables. y^* changes similarly for the multijet background and the signal.

3.2 \vec{p}_T^{miss} Decomposition

The challenge in this search is reconstructing the multiple missing transverse momentum contributions that arise from the production of stable bound states during the dark quark hadronization. We compare multiple methods of decomposing the measured \vec{p}_T^{miss} two-vector into components matching the two semi-visible jets in each event.

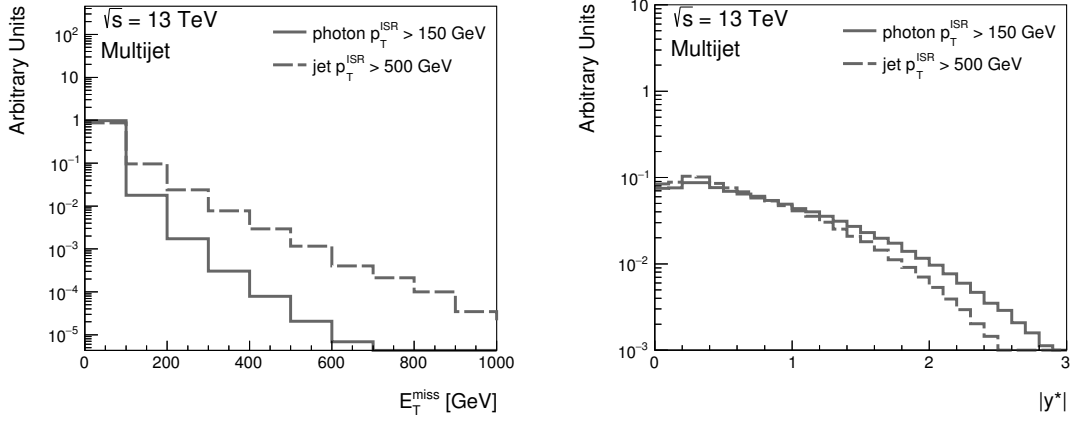


Figure 4: E_T^{miss} (left) and $|y^*|$ (right) distributions of multijet events for $p_T^{\text{ISR}} = 150$ GeV (solid line) and $p_T^{\text{ISR}} = 500$ GeV (dashed line).

The first method is the calculation of the m_{T2} mass variable [35] (computed using Ref. [36]). m_{T2} is defined as:

$$m_{T2} \equiv \min \left[\max \left\{ m_T(j_1, \vec{p}_T^{\text{miss}_1}), m_T(j_2, \vec{p}_T^{\text{miss}_2}) \right\} \right], \quad (3.1)$$

where the minimization considers all possible values satisfying:

$$\vec{p}_T^{\text{miss}} = \vec{p}_T^{\text{miss}_1} + \vec{p}_T^{\text{miss}_2}, \quad (3.2)$$

and the transverse mass m_T is defined as:

$$m_T^2(j, \vec{p}_T^{\text{miss}}) = (E_T^j + E_T^{\text{miss}})^2 - (\vec{p}_T^j + \vec{p}_T^{\text{miss}})^2. \quad (3.3)$$

This method was developed for any final-state system with two invisible particles. It naturally produces two missing transverse momentum components, each associated with one of the two jets included in the calculation.

A newer, analytic decomposition was developed specifically for semivisible jet final states [37]. This technique assumes that the visible and invisible transverse momentum of each semivisible jet are aligned. The ratio between the visible and invisible transverse momentum is strongly correlated with $r_{\text{inv}}/(1 - r_{\text{inv}})$. This leads to the following system of equations that can be solved to find the two coefficients α_1 and α_2 , using Eq. (3.2) as a constraint:

$$\vec{p}_T^{\text{miss}_1} = \alpha_1 \cdot \vec{p}_T^{j_1}, \quad (3.4)$$

$$\vec{p}_T^{\text{miss}_2} = \alpha_2 \cdot \vec{p}_T^{j_2}. \quad (3.5)$$

3.3 Mass Reconstruction

The transverse mass m_T , with the visible component as the massive dijet system, was proposed in Ref. [20] and used in the CMS s -channel search [22] to reconstruct the Z' mediator

mass. By default, the multijet background distribution for this type of mass variable has a smoothly falling spectrum, facilitating background estimation. Simply requiring large E_T^{miss} sculpts the background m_T distribution significantly, motivating the introduction of r_T , the ratio between E_T^{miss} and m_T , which was shown to bring a clear sensitivity gain with minimal background sculpting.

Another, more sophisticated method to recover the Z' mass uses the m_{T2} construction: the m_{T2} -assisted on shell (MAOS) technique [38]. MAOS produces the variable m_{MAOS} by promoting the decomposed two-vectors $\vec{p}_T^{\text{miss}1}$ and $\vec{p}_T^{\text{miss}2}$ to four-vectors, assigning $p_z^{\text{miss}1} = p_z^{j1} (p_T^{\text{miss}1}/p_T^{j1})$ and $m^{\text{miss}1} = 0$, and similarly for the second component. The invariant mass of the two visible four-vectors and the two invisible four-vectors is then an estimate of the mediator mass. This variable was recently shown to be nearly optimal in Ref. [39] for SVJ searches without any ISR.

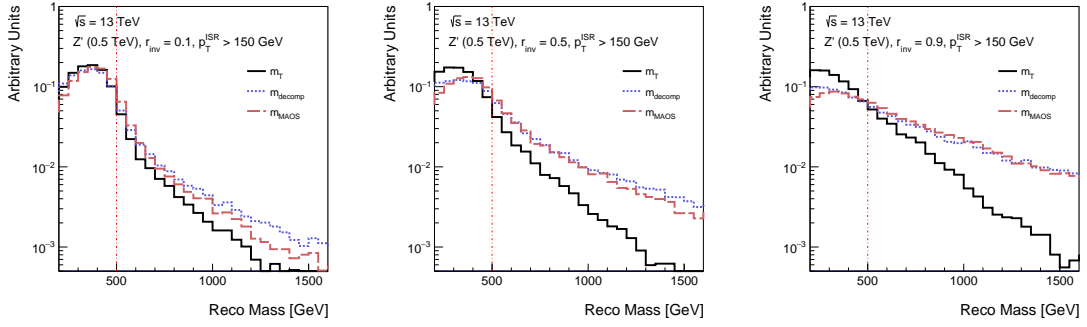


Figure 5: Distributions of different reconstructed mass variables for $m_{Z'} = 0.5$ TeV with $p_T^{\text{ISR}} = 150$ GeV and $r_{\text{inv}} = 0.1$ (left), $r_{\text{inv}} = 0.5$ (center), and $r_{\text{inv}} = 0.9$ (right). The red dashed vertical line shows the theoretical $m_{Z'}$ value.

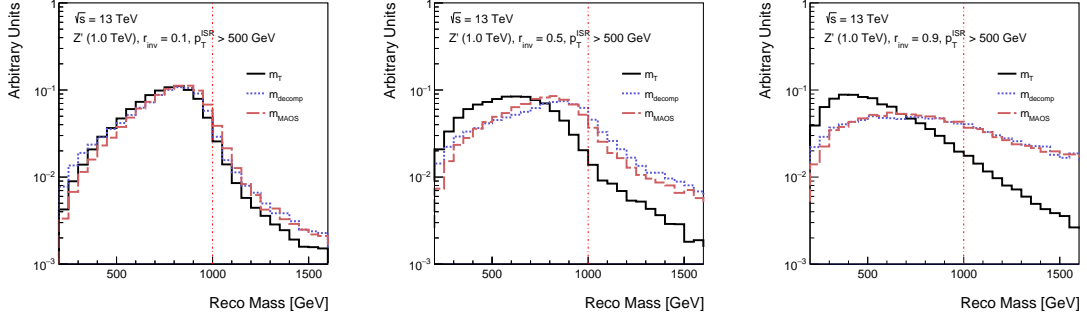


Figure 6: Distributions of different reconstructed mass variables for $m_{Z'} = 1.0$ TeV with $p_T^{\text{ISR}} = 500$ GeV and $r_{\text{inv}} = 0.1$ (left), $r_{\text{inv}} = 0.5$ (center), and $r_{\text{inv}} = 0.9$ (right). The red dashed vertical line shows the theoretical $m_{Z'}$ value.

We apply the same procedure to the invisible components from the analytic decomposition, resulting in the new variable m_{decomp} . This combination has not been studied

before. We compare all three mass variables for $m_{Z'} = 0.5$ TeV with $p_T^{\text{ISR}} = 150$ GeV in Figure 5 and for $m_{Z'} = 1.0$ TeV with $p_T^{\text{ISR}} = 500$ GeV in Figure 6. For this comparison, we assume that the semivisible jets in each event are always correctly identified (further discussed in Section 4.1). Both m_{MAOS} and m_{decomp} retain better performance than m_T as r_{inv} increases. m_{MAOS} is found to have the best resolution. Importantly, all three variables have similarly falling spectra in multijet background events.

3.4 r_{inv} Reconstruction

We further extend the use of \vec{p}_T^{miss} decomposition techniques to measure r_{inv} on a per-event basis. This is most natural for the analytic decomposition, which is explicitly based on r_{inv} . In this case, we can write $r_{\text{inv}}^i = \alpha_i / (1 + \alpha_i)$ for jet i , and we observe that the signal events tend to have larger r_{inv}^i for both jets. As a consequence, \bar{r}_{inv} , the average of r_{inv}^i , can be used to distinguish signal events from the background. The \bar{r}_{inv} is smaller than the corresponding r_{inv} for various reasons. Events are already required to have two jets with $p_T > 25$ GeV, which acts as a requirement on the visible decay fraction in each jet. In addition, the jet axes are only approximations of the invisible components.

To apply the same principle to the numerical m_{T2} decomposition, we must account for the lack of an explicit α coefficient relating the x and y momenta of each invisible component. We therefore take the average of the corresponding formula applied separately to the x and y momenta:

$$r_{\text{inv}}^i = \frac{1}{2} \left(\frac{p_x^{\text{miss}_i}}{p_x^{j_i} + p_x^{\text{miss}_i}} + \frac{p_y^{\text{miss}_i}}{p_y^{j_i} + p_y^{\text{miss}_i}} \right). \quad (3.6)$$

We then define the average \bar{r}_{inv}' in the same way as \bar{r}_{inv} above.

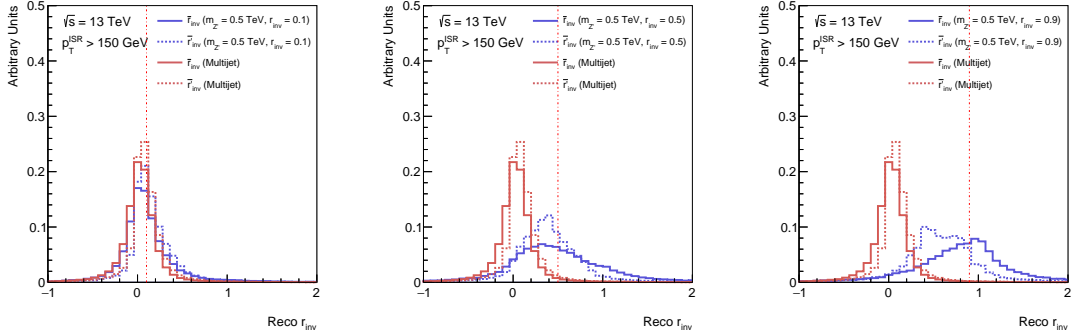


Figure 7: Distributions of r_{inv} estimators for the multijet background and signals with $m_{Z'} = 0.5$ TeV, $p_T^{\text{ISR}} = 150$ GeV, and $r_{\text{inv}} = 0.1$ (left), $r_{\text{inv}} = 0.5$ (center), and $r_{\text{inv}} = 0.9$ (right). The red dashed vertical line shows the theoretical r_{inv} value.

Comparisons between these two r_{inv} estimators are shown in Figures 7 and 8, and their average values are compared to the theoretical r_{inv} value (specified during signal simulation) in Fig. 9. As r_{inv} increases, both variables become more powerful. However,

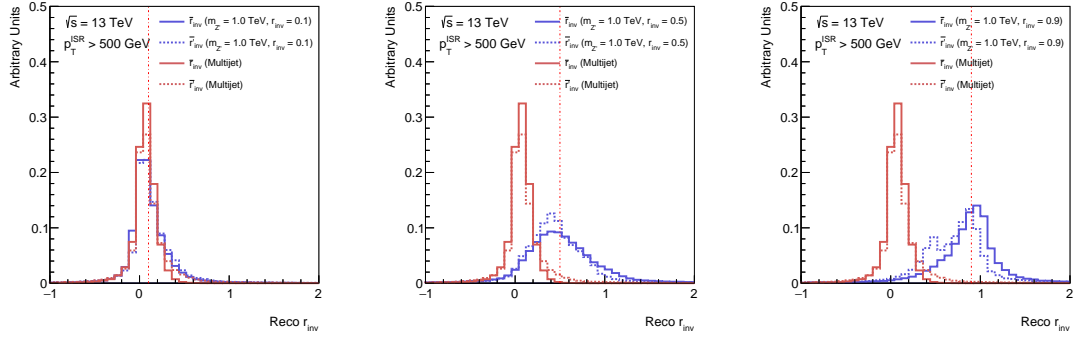


Figure 8: Distributions of r_{inv} estimators for the multijet background and signals with $m_{Z'} = 1.0$ TeV, $p_{\text{T}}^{\text{ISR}} = 500$ GeV, and $r_{\text{inv}} = 0.1$ (left), $r_{\text{inv}} = 0.5$ (center), and $r_{\text{inv}} = 0.9$ (right). The red dashed vertical line shows the theoretical r_{inv} value.

as studied later in Section 4.3, \bar{r}'_{inv} is not as powerful as \bar{r}_{inv} . There is a clear relationship with the theoretical r_{inv} value, which could be used for calibration when measuring this quantity. Both \bar{r}_{inv} and r_{T} can be used to enhance sensitivity, as will be investigated in Section 4.

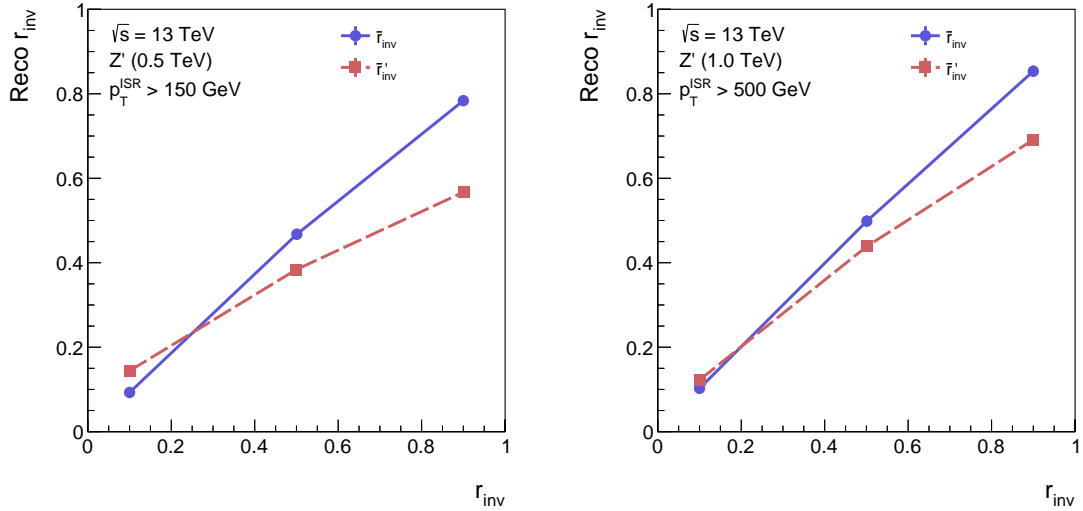


Figure 9: Comparisons of the average values of the two r_{inv} estimators with the theoretical r_{inv} value, for signals with $m_{Z'} = 0.5$ TeV, $p_{\text{T}}^{\text{ISR}} = 150$ GeV (right) and $m_{Z'} = 1.0$ TeV, $p_{\text{T}}^{\text{ISR}} = 500$ GeV (left).

3.5 Combining Observables

As both \bar{r}_{inv} and m_{MAOS} have excellent discriminating power, combining the two may further enhance the search power. Figure 10 shows the $m_{\text{MAOS}}-\bar{r}_{\text{inv}}$ 2D distribution for both the multijet background and the signal. The signal events are clustered in the region

determined by the Z' mass and r_{inv} . This opens up new ways to perform this search, as discussed in Section 5.

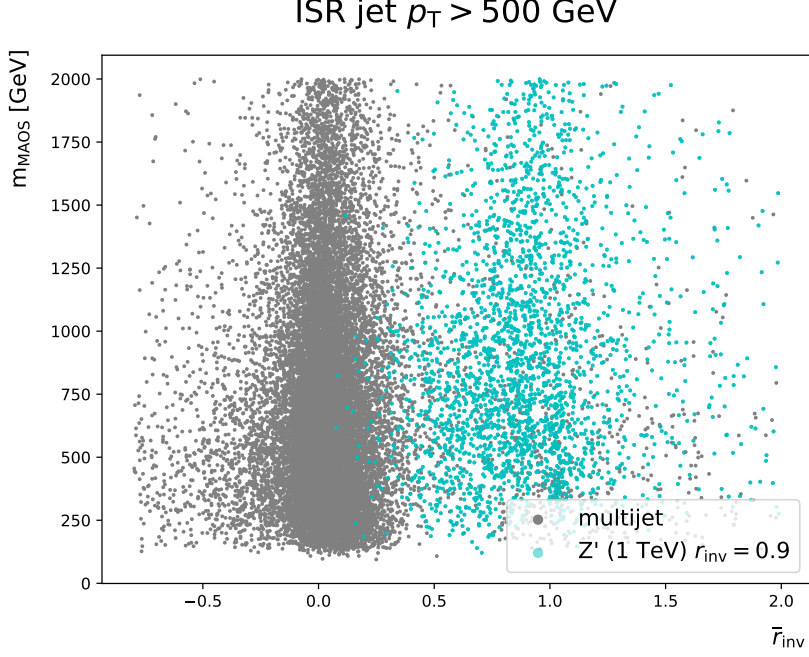


Figure 10: Scatterplot of m_{MAOS} and \bar{r}_{inv} for multijet (grey, 20000 events) and Z' (cyan, 10000 events). The Z' sample has a mass of 1 TeV and an r_{inv} parameter of 0.9. The ISR jet is required to have $p_{\text{T}} > 500$ GeV.

Similar to m_{T} , m_{MAOS} and \bar{r}_{inv} benefit from the energetic ISR object. The performance of \bar{r}_{inv} drops dramatically as the p_{T} of the ISR object decreases. This is because the decomposition is influenced by the angular separation. This can be clearly appreciated from an extreme example where $\vec{p}_{\text{T}}^{\text{miss}}$ is perfectly aligned with one of the jets. In this situation, the decomposition is ambiguous unless the system is boosted.

This event-level topology can be generalized as a two-body decay with non-interacting final state particles in each decay leg. This behavior is expected in various scenarios such as leptonic $H \rightarrow \tau^+\tau^-$ and $H \rightarrow W^+W^-$ decays. Methods proposed to improve reconstruction of the Higgs mass in semivisible decays can be applied to SVJs as well; in fact, this was the original genesis of the MAOS method. The performance improvement in collinear events has also been discussed in the context of $H \rightarrow \tau^+\tau^-$ [40]. SVJ searches will likely benefit further from more interactions between various communities.

4 Analysis Strategy

In this section, we demonstrate the feasibility of constructing a search for a resonant Z' decaying to dark quarks in the ISR production channels, where the two jets originating from the dark quarks are reconstructed as two separated small-radius ($R = 0.5$) jets. When

the Z' mass is very small, using large-radius jets containing the entire boosted Z' system is a better choice, but this is a different strategy not pursued here.

4.1 Jet Matching Method

Experimentally, the two jets from Z' have to be distinguished from the ISR object. In the photon ISR case, simply selecting the leading two jets is sufficient. However, as reported in other resonance searches using an ISR jet, the jet matching is a challenging task. In particular, once the ISR jet and the two jets from the heavy particles have similar p_T , the three jets are well balanced on the transverse plane, forming a triangular topology. It is extremely difficult to disentangle these three jets using basic kinematic properties only. In SVJ models, thanks to the appreciable E_T^{miss} , we are able to identify the two signal jets using $\Delta\phi$ between the jet pair and \vec{p}_T^{miss} , as illustrated in Figure 11. Since the two target jets and E_T^{miss} come from the Z' , when the Z' system is boosted, these three objects are collimated, resulting in smaller separations in $\Delta\phi$. While identifying the correct jets in signal events is critical, ensuring minimal background sculpting is equally important. It is found that minimizing the variable $(\Delta\phi_{j_i, j_k} + \Delta\phi_{j_i j_k, \vec{p}_T^{\text{miss}}})/2$ gives a smooth background and acceptable matching efficiency. $\Delta\phi_{j_i, j_k}$ is the $\Delta\phi$ between two jets under consideration, and $\Delta\phi_{j_i j_k, \vec{p}_T^{\text{miss}}}$ is the $\Delta\phi$ between the corresponding dijet system and \vec{p}_T^{miss} . Before the minimization, the three jets are required to be well-separated by requiring $\Delta\phi$ between each pair to be larger than 0.8. The two jets from the Z' , j_1 and j_2 , are identified by matching the dark quarks to reconstructed jets by requiring $\Delta R < 0.4$ in order to evaluate the efficiency.

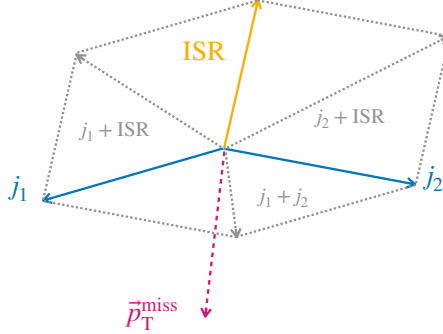


Figure 11: Transverse view of the two jets, ISR object and \vec{p}_T^{miss} .

Figure 12 shows the probabilities of different jet pairs to be selected via the above procedure. As the p_T of the ISR jet increases, the matching efficiency of this method improves. For 500 GeV, the method is over 90% efficient for large r_{inv} values.

4.2 Basic Selections

The typical threshold for a single isolated photon trigger is about 140 GeV, while the corresponding threshold for a single jet trigger is about 420 GeV [29]. Therefore, the events are categorized into two channels: one requires an energetic photon with $p_T > 150$ GeV,

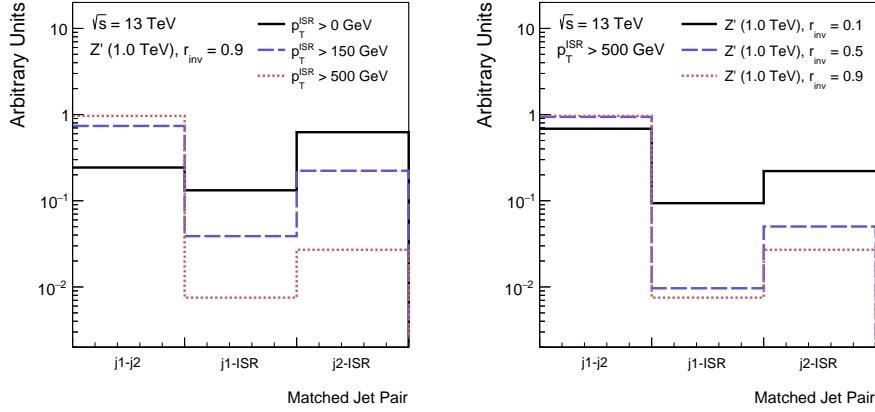


Figure 12: Fractions of various matching configurations for one Z' sample with different ISR p_T selections (left), and for three Z' samples with different r_{inv} parameters when the same ISR p_T selection is applied (right). The first bin on the x -axis corresponds to the case where the matching procedure correctly identifies the two jets from the Z' .

and the other requires a jet with p_T larger than 500 GeV. The thresholds are slightly increased so that the analysis considers events above the trigger turn-on region.

Furthermore, the events are required to contain at least two (three) $R = 0.5$ jets clustered with the anti- k_T algorithm [41, 42], passing $p_T > 25$ GeV, with $|\eta| < 4.5$, for the photon (jet) ISR channel. (The choice of jet clustering radius is discussed further in Appendix A.) In the photon channel, the photon must not overlap with the two leading jets ($\Delta R > 0.4$). The two signal jets are identified as the leading two jets in the photon ISR channel, and the two signal jets are identified via the method mentioned above in the jet ISR channel. The $|y^*|$ variable has been used in numerous dijet resonance searches in the past, so a similar strategy is adopted here. The threshold is chosen to be 0.8, based on a recently published ATLAS result [29] that considers similar kinematic regions.

4.3 Signal Region Categorization

As discussed in Section 3, both \bar{r}_{inv} and \bar{r}'_{inv} have excellent discriminating power for signal with large r_{inv} . Here, we also compare these variables to r_T , since they all involve the E_T^{miss} , though in different ways. The approximate significance S/\sqrt{B} , based on the signal and background yields S and B , is evaluated for a range of values in each variable. The signal yields S and B are evaluated for $1/2 m_{Z'} < m_{\text{MAOS}} < 3/2 m_{Z'}$, in order to consider the most pertinent background events in the region near the signal mass peak, which provides the most sensitivity. Figure 13 shows the results for the 0.5 (1.0) TeV Z' in the photon (jet) ISR channels. In the photon ISR channel where the boost is modest, r_T brings better sensitivity, while in the jet ISR channel, \bar{r}_{inv} performs the best except in the very high signal efficiency region. This is expected as \bar{r}_{inv} is more impacted by the boost. It is also clear that \bar{r}'_{inv} is not as efficient as \bar{r}_{inv} in the jet ISR channel.

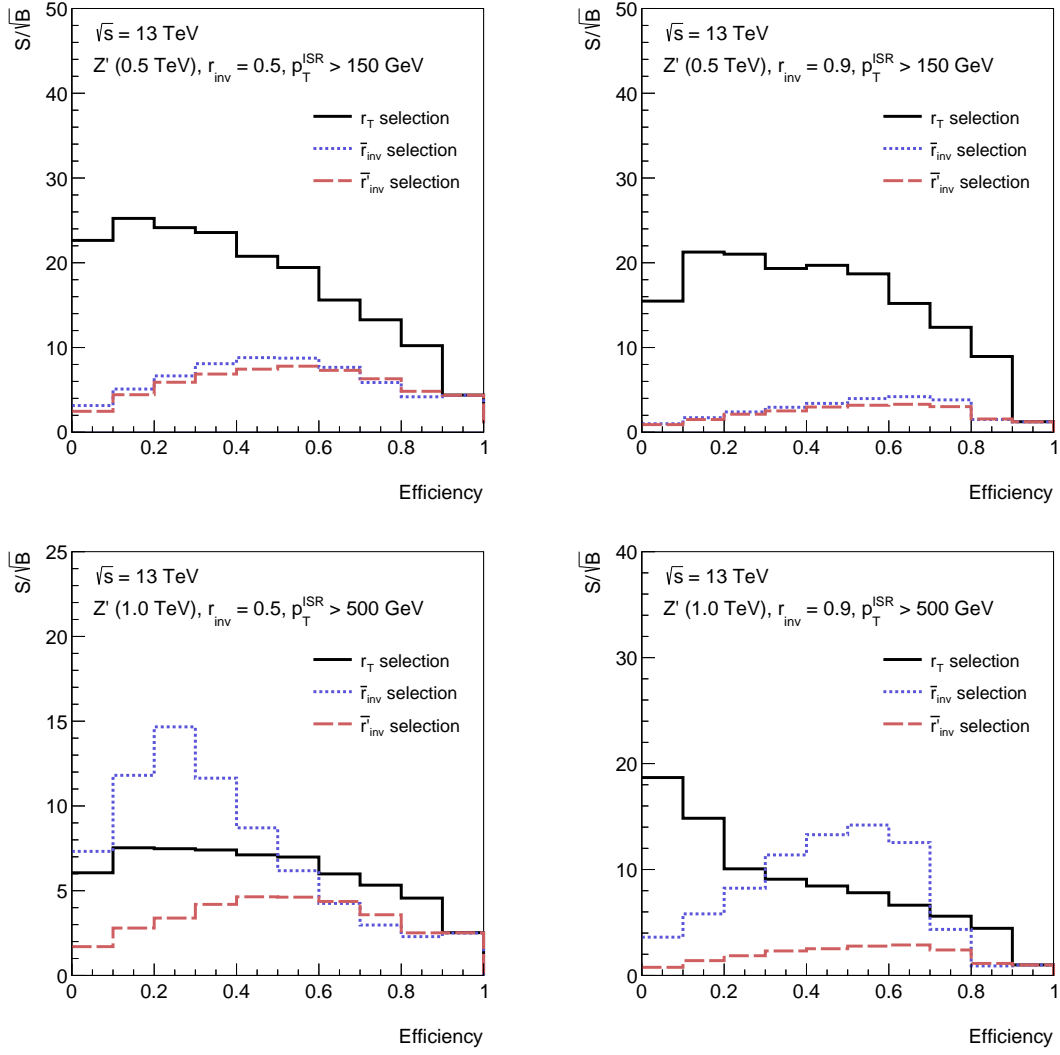


Figure 13: Top: Significance in the photon ISR channel as a function of the signal efficiency for selections on r_T , \bar{r}_{inv} , or \bar{r}'_{inv} . The 0.5 TeV Z' samples with an r_{inv} parameter of 0.5 (left) and 0.9 (right) are considered. Bottom: Significance in the jet ISR channel as a function of the signal efficiency for selections on r_T , \bar{r}_{inv} , or \bar{r}'_{inv} . The 1.0 TeV Z' samples with an r_{inv} parameter of 0.5 (left) and 0.9 (right) are considered.

The photon and jet ISR channels are optimized separately using r_T and \bar{r}_{inv} , respectively, as presented in Figure 14. We apply a cut at 0.4 on r_T (\bar{r}_{inv}) in the photon (jet) ISR channels to estimate the final sensitivity. In principle, tighter selections on r_T (\bar{r}_{inv}) can be applied, but the reduced background efficiency leads to unacceptable statistical uncertainty in the generated background sample. Table 2 summarizes all the selections applied to achieve the final results. The minimum m_{MAOS} selections for each channel are necessary to ensure a smoothly falling background spectrum. For lower m_{MAOS} values,

the multijet background has a peak, arising from Sudakov suppression [43] and any other sculpting from kinematic selections.

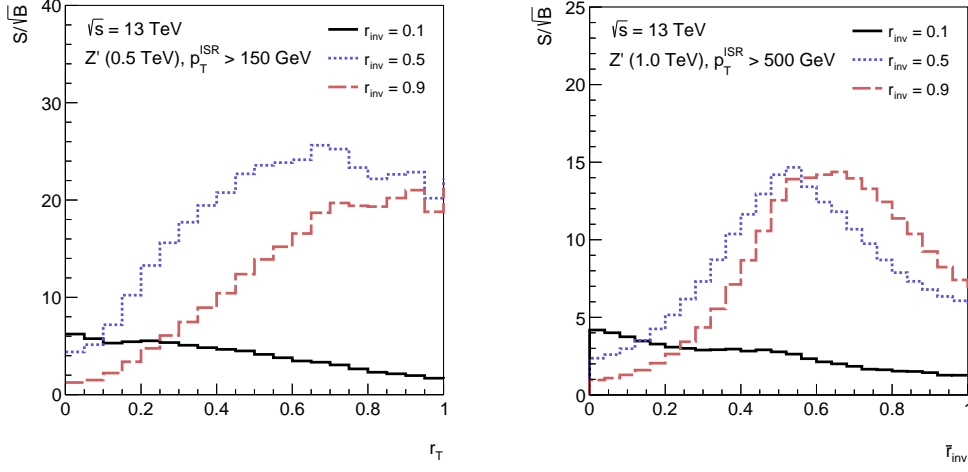


Figure 14: Significance as a function of r_T (left) and \bar{r}_{inv} (right) for the photon ISR channel and jet ISR channel, respectively. In the photon (jet) ISR channel, the 0.5 (1.0) TeV Z' sample is studied with three r_{inv} values.

Table 2: The complete set of signal region selections applied to both the photon ISR and jet ISR channels.

Photon ISR	Jet ISR
≥ 1 photon with $p_T > 150$ GeV	≥ 1 Jet with $p_T > 500$ GeV
≥ 2 jets with $p_T > 25$ GeV, $ \eta < 4.5$	≥ 3 jets with $p_T > 25$ GeV, $ \eta < 4.5$
Jet-photon overlap removal	-
Leading two jets as signal jets	Identify two signal jets via jet matching
$ y^* < 0.8$	
$r_T > 0.4$	$\bar{r}_{\text{inv}} > 0.4$
$m_{\text{MAOS}} > 200$ GeV	$m_{\text{MAOS}} > 400$ GeV

5 Sensitivity Estimation

The traditional background modeling method is to perform a fit to data, as in the CMS analysis [22]. Here we present the ideal sensitivities given perfect background modeling. Since we have identified m_{MAOS} as a better observable, the sensitivities are presented as functions of m_{MAOS} . We apply the selections in Table 2, optimized separately for each channel as discussed in Section 4.3. As seen in Figure 15, thanks to the \bar{r}_{inv} (r_T)

selection, the significance is increased by up to a factor of ten across the bulk of the m_{MAOS} distribution for 1.0 (0.5) TeV Z' with $r_{\text{inv}} = 0.9$ in the jet (photon) ISR channel.

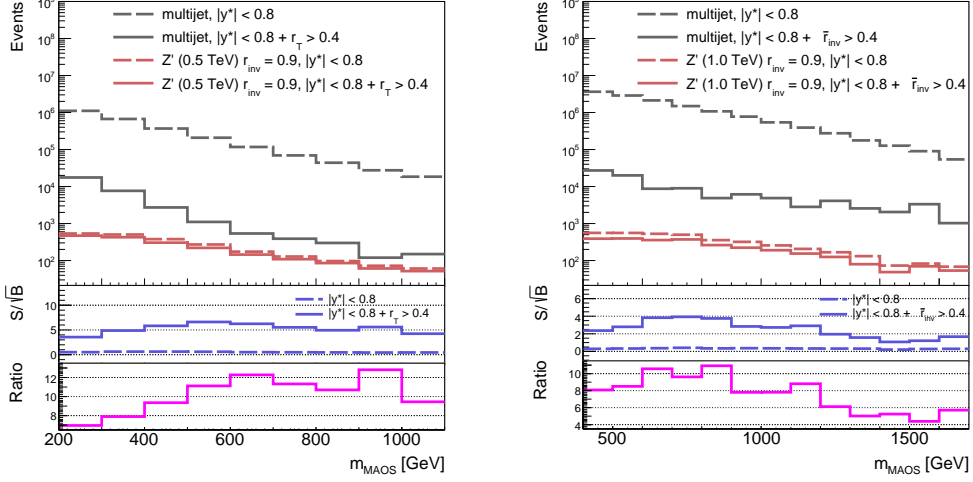


Figure 15: Signal and background distributions in the photon ISR (left) and jet ISR (right) signal regions. The significance is compared between the signal region selections with and without the r_T (left) or the \bar{r}_{inv} (right) requirements. The bottom panel presents the ratio between the significance curves in the middle panel.

The fact that \bar{r}_{inv} is a reasonable estimator of r_{inv} , forming a localized feature, motivates an exploration of using its full distribution rather than just as a selection. Figure 16 shows the significance in the $m_{\text{MAOS}}-\bar{r}_{\text{inv}}$ 2D plane, for the 1 TeV Z' with various r_{inv} parameters, where a local peak is formed in each case. Scanning this 2D plane is a viable search strategy. However, the background modeling is more challenging. Figures 7 and 8 show that the \bar{r}_{inv} distribution is smooth in both multijet and signal, which makes it possible to model this variable via a parameterization. Another advantage of this approach is that it provides a unified strategy for various r_{inv} and mass combinations without choosing a particular \bar{r}_{inv} selection.

The sensitivity can be further quantified by computing the limits on $\sigma_{Z'}\mathcal{B}(Z' \rightarrow \chi\bar{\chi})$ at the 95% confidence level (CL) using the asymptotic approximation to the CL_s method [44]. The expected limits from both the 1D and 2D approaches are evaluated for the jet ISR channel, as a function of the Z' mass. Two additional signal mass points, 750 GeV and 1250 GeV, are added to show the trend. The exclusion limits are calculated in PYHF 0.7.6 [45, 46], where the background estimate is taken directly from the simulated multijet samples. In the 1D approach, the m_{MAOS} distribution after applying the $\bar{r}_{\text{inv}} > 0.4$ selection is considered, while the 2D approach utilizes the entire $m_{\text{MAOS}}-\bar{r}_{\text{inv}}$ 2D plane¹. Figure 17 compares the expected limits between these two strategies, which clearly motivates further development

¹PYHF 0.7.6 currently does not support an optimal 2D treatment, where the correlations between neighboring bins are all taken into account. The 2D input is flattened into a 1D dataset, i.e. a list of values in the $\bar{r}_{\text{inv}}-m_{\text{MAOS}}$ bins.

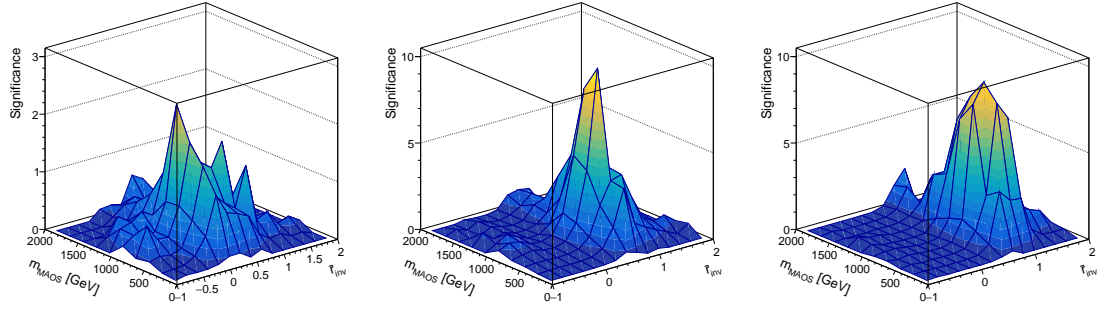


Figure 16: The significance distribution in the $m_{\text{MAOS}}-\bar{r}_{\text{inv}}$ plane in the jet ISR channel for the 1.0 TeV Z' with $r_{\text{inv}} = 0.1$ (left), 0.5 (middle) and 0.9 (right).

of the 2D approach.

The absolute experimental accuracy of this study is subject to limitations in detector and reconstruction modeling in Delphes. Jets misidentified as photons will complicate the event selection in the ISR photon channel, potentially leading to additional backgrounds or reduced matching efficiency. Mismeasured jets will induce spurious \vec{p}_T^{miss} , increasing the multijet background. However, the relative performance of the different strategies for the different signal models is accurately reflected here.

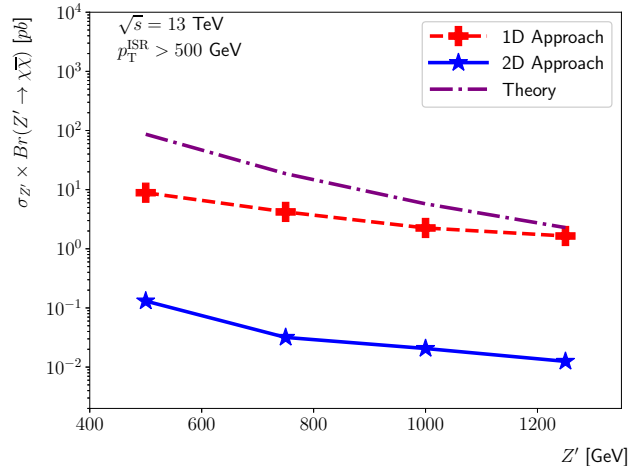


Figure 17: Expected limits at 95% CL obtained in the jet ISR channel, as functions of the Z' mass. The 1D approach (dashed line) applies the $\bar{r}_{\text{inv}} > 0.4$ cut before scanning the m_{MAOS} spectrum, and the 2D approach (solid line) directly considers the $m_{\text{MAOS}}-\bar{r}_{\text{inv}}$ 2D plane. The predicted $\sigma_{Z'}\mathcal{B}$ from MADGRAPH5_aMC@NLO 3.5.1 [30] is also displayed (dashed dotted line).

6 Outlook

This work considers the case where two semi-visible jets (SVJs) are produced along with initial state radiation (ISR), proving that this production channel is a promising avenue for semi-visible jet searches. Besides allowing us to overcome the trigger threshold limitation, the presence of an energetic ISR object brings other advantages. We derive several observables to reconstruct properties of the semi-visible jet process that show great potential. Assuming that each invisible decay component is aligned with the corresponding visible jet, an analytic \vec{p}_T^{miss} decomposition facilitates an estimation of the invisible fraction for each jet, which can be averaged to find the event-level invisible fraction \bar{r}_{inv} . The separation power of this observable is enhanced as the ISR p_T increases. The reconstructed mediator mass m_{MAOS} is found using a different, numerical \vec{p}_T^{miss} decomposition based on m_{T2} and promoting the two invisible components to four-vectors with the m_{T2} -assisted on shell (MAOS) scheme [38]. The signal m_{MAOS} resolution suffers almost no degradation as r_{inv} increases, when the ISR p_T is significant. In addition, the matching ambiguity in the jet ISR channel is mitigated thanks to the alignment of E_T^{miss} with the signal jets, and we propose a method that gives good matching efficiency with minimal background distortion.

The analysis sensitivity is studied in detail for a 0.5 (1.0) TeV Z' with $r_{\text{inv}} = 0.9$ in the photon (jet) ISR channel. If only m_{MAOS} is used as the search variable, the sensitivity can be greatly increased by cutting on the ratio of E_T^{miss} and m_T (\bar{r}_{inv}). Further, the \bar{r}_{inv} of the signal is similarly localized, so a search in the $m_{\text{MAOS}}\text{-}\bar{r}_{\text{inv}}$ 2D plane merits investigation. A preliminary examination of the expected limits shows that the 2D approach is an order of magnitude more sensitive. This conclusion applies to mediator masses below 1 TeV and other r_{inv} values as well. Observables constructed using E_T^{miss} are not invariant with respect to the ISR object p_T , so a thorough survey is needed to optimize the search strategy. This analysis is complementary to the s -channel SVJ search performed by CMS [22] as it covers mediator masses below 1.5 TeV. The proposed 2D approach is expected to achieve better sensitivity than a traditional monojet search [7, 8], thanks to the dedicated new observables.

It is possible to apply a unified search strategy to explore a wide range of the r_{inv} model parameter using the techniques developed in this work. Even when r_{inv} approaches unity, a mass resonance can be reconstructed. As recently pointed out in Ref. [47], jet substructure variables suffer from large modeling uncertainties in the context of dark QCD. This study explores only simple physics objects, which makes it applicable to various showering models. The advantages of jet substructure variables and machine learning in SVJ searches were studied by previous publications [22, 48–52], and the findings in this work could be combined with those methods. In particular, a single \vec{p}_T^{miss} decomposition that provides optimal reconstruction for both the mediator mass and invisible fraction could potentially be achieved using interpretable machine learning [39]. We point out that the event-level topological features are similar between SVJ and other processes such as Higgs decays with both visible and invisible final state particles. We look forward to seeing the ISR production channels probed in SVJ searches by the LHC experiments.

Acknowledgments

We thank Benedikt Maier and Brendan Regnery for initial discussions on this topic. B.X. Liu is supported by Shenzhen Campus of the Sun Yat-sen University under project 74140-12240013. B.X. Liu appreciates the support from Guangdong Provincial Key Laboratory of Gamma-Gamma Collider and Its Comprehensive Applications, and the support from Guangdong Provincial Key Laboratory of Advanced Particle Detection Technology. K. Pedro is supported by Fermi Research Alliance, LLC under Contract No. DE-AC02-07CH11359 with the U.S. Department of Energy, Office of Science, Office of High Energy Physics.

A Impacts of the Jet Clustering Radius

As mentioned in Section 1, many dark hadrons are created during dark shower, a fraction of which subsequently decay to SM quarks. The width of the jet increases with the dark hadron mass, as heavier dark hadrons impart more momentum to their decay products, leading to wider opening angles. This effect was reported in Ref. [22], where $R = 0.8$ jets were used to achieve better performance. The impacts of the jet clustering radius are investigated for the ISR topology in this work. Five different clustering radii are considered from $R = 0.4$ to $R = 0.8$ with a step of 0.1. We label these different jet types as AK4 to AK8, since they all use anti- k_T clustering.

As shown in Fig. 18, the impact of the jet clustering radius on m_{MAOS} is obvious at low r_{inv} . However, as r_{inv} increases, E_T^{miss} becomes more important and the impact of the clustering radius decreases. The m_{MAOS} distribution is not significantly affected when $r_{\text{inv}} = 0.9$. The new \bar{r}_{inv} observable proposed in this work is not affected by the jet clustering radius, as seen in Fig. 19, for the same reasons. Therefore, the results in this paper apply to various jet clustering choices.

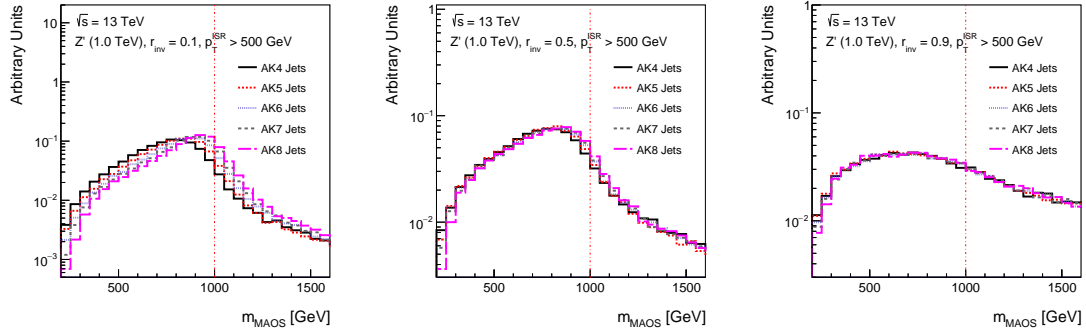


Figure 18: Distributions of m_{MAOS} for signals with $m_{Z'} = 1.0$ TeV, $p_T^{\text{ISR}} = 500$ GeV, and $r_{\text{inv}} = 0.1$ (left), $r_{\text{inv}} = 0.5$ (center), and $r_{\text{inv}} = 0.9$ (right), using various jet clustering radii. The red dashed vertical line shows the actual Z' mass.

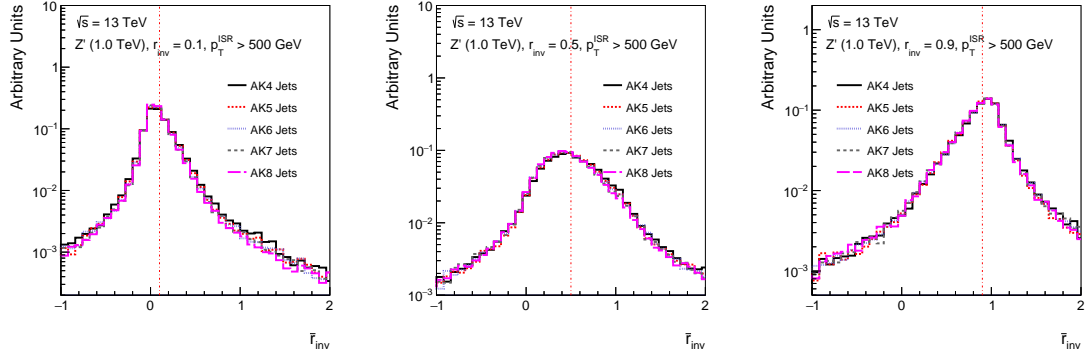


Figure 19: Distributions of r_{inv} estimator for signals with $m_{Z'} = 1.0$ TeV, $p_T^{\text{ISR}} = 500$ GeV, and $r_{\text{inv}} = 0.1$ (left), $r_{\text{inv}} = 0.5$ (center), and $r_{\text{inv}} = 0.9$ (right), using various jet clustering radii. The red dashed vertical line shows the theoretical r_{inv} value.

References

- [1] V.C. Rubin, N. Thonnard and W.K. Ford, Jr., *Rotational properties of 21 SC galaxies with a large range of luminosities and radii, from NGC 4605 /R = 4kpc/ to UGC 2885 /R = 122 kpc/, [Astrophys. J.](#) **238** (1980) 471.*
- [2] M. Persic, P. Salucci and F. Stel, *The universal rotation curve of spiral galaxies: 1. the dark matter connection, [Mon. Not. Roy. Astron. Soc.](#) **281** (1996) 27 [[astro-ph/9506004](#)].*
- [3] D. Clowe, M. Bradac, A.H. Gonzalez, M. Markevitch, S.W. Randall, C. Jones et al., *A direct empirical proof of the existence of dark matter, [Astrophys. J. Lett.](#) **648** (2006) L109 [[astro-ph/0608407](#)].*
- [4] DES collaboration, *Dark Energy Survey year 1 results: Curved-sky weak lensing mass map, [Mon. Not. Roy. Astron. Soc.](#) **475** (2018) 3165 [[1708.01535](#)].*
- [5] PLANCK collaboration, *Planck 2018 results. VI. Cosmological parameters, [Astron. Astrophys.](#) **641** (2020) A6 [[1807.06209](#)].*
- [6] G. Jungman, M. Kamionkowski and K. Griest, *Supersymmetric dark matter, [Phys. Rept.](#) **267** (1996) 195 [[hep-ph/9506380](#)].*
- [7] CMS collaboration, *Search for new particles in events with energetic jets and large missing transverse momentum in proton-proton collisions at $\sqrt{s} = 13$ TeV, [JHEP](#) **11** (2021) 153 [[2107.13021](#)].*
- [8] ATLAS collaboration, *Search for new phenomena in events with an energetic jet and missing transverse momentum in pp collisions at $\sqrt{s} = 13$ TeV with the ATLAS detector, [Phys. Rev. D](#) **103** (2021) 112006 [[2102.10874](#)].*
- [9] CMS collaboration, *Search for dark matter produced in association with a single top quark or a top quark pair in proton-proton collisions at $\sqrt{s} = 13$ TeV, [JHEP](#) **03** (2019) 141 [[1901.01553](#)].*
- [10] ATLAS collaboration, *Search for new phenomena in events with two opposite-charge leptons, jets and missing transverse momentum in pp collisions at $\sqrt{s} = 13$ TeV with the ATLAS detector, [JHEP](#) **04** (2021) 165 [[2102.01444](#)].*
- [11] ATLAS collaboration, *Search for new phenomena with top quark pairs in final states with one lepton, jets, and missing transverse momentum in pp collisions at $\sqrt{s} = 13$ TeV with the ATLAS detector, [JHEP](#) **04** (2021) 174 [[2012.03799](#)].*
- [12] CMS collaboration, *Search for dark matter produced in association with a leptonically decaying Z boson in proton-proton collisions at $\sqrt{s} = 13$ TeV, [Eur. Phys. J. C](#) **81** (2021) 13 [[2008.04735](#)].*
- [13] ATLAS collaboration, *Search for dark matter in events with a hadronically decaying vector boson and missing transverse momentum in pp collisions at $\sqrt{s} = 13$ TeV with the ATLAS detector, [JHEP](#) **10** (2018) 180 [[1807.11471](#)].*
- [14] CMS collaboration, *Search for new physics in final states with a single photon and missing transverse momentum in proton-proton collisions at $\sqrt{s} = 13$ TeV, [JHEP](#) **02** (2019) 074 [[1810.00196](#)].*
- [15] CMS collaboration, *Search for dark matter produced in association with a Higgs boson decaying to a pair of bottom quarks in proton-proton collisions at $\sqrt{s} = 13$ TeV, [Eur. Phys. J. C](#) **79** (2019) 280 [[1811.06562](#)].*

- [16] ATLAS collaboration, *Search for dark matter produced in association with a Higgs boson decaying to tau leptons at $\sqrt{s} = 13$ TeV with the ATLAS detector*, *JHEP* **09** (2023) 189 [[2305.12938](#)].
- [17] ATLAS collaboration, *Search for dark matter produced in association with a Standard Model Higgs boson decaying into b-quarks using the full Run 2 dataset from the ATLAS detector*, *JHEP* **11** (2021) 209 [[2108.13391](#)].
- [18] Y. Bai and P. Schwaller, *Scale of dark QCD*, *Phys. Rev. D* **89** (2014) 063522 [[1306.4676](#)].
- [19] H. Beauchesne, E. Bertuzzo and G. Grilli Di Cortona, *Dark matter in hidden valley models with stable and unstable light dark mesons*, *JHEP* **04** (2019) 118 [[1809.10152](#)].
- [20] T. Cohen, M. Lisanti and H.K. Lou, *Semivisible jets: Dark matter undercover at the LHC*, *Phys. Rev. Lett.* **115** (2015) 171804 [[1503.00009](#)].
- [21] T. Cohen, M. Lisanti, H.K. Lou and S. Mishra-Sharma, *LHC searches for dark sector showers*, *JHEP* **11** (2017) 196 [[1707.05326](#)].
- [22] CMS collaboration, *Search for resonant production of strongly coupled dark matter in proton-proton collisions at 13 TeV*, *JHEP* **06** (2022) 156 [[2112.11125](#)].
- [23] ATLAS collaboration, *Search for non-resonant production of semi-visible jets using Run 2 data in ATLAS*, *Phys. Lett. B* **848** (2024) 138324 [[2305.18037](#)].
- [24] G. Albouy et al., *Theory, phenomenology, and experimental avenues for dark showers: a Snowmass 2021 report*, *Eur. Phys. J. C* **82** (2022) 1132 [[2203.09503](#)].
- [25] ATLAS collaboration, *Search for resonant production of dark quarks in the dijet final state with the ATLAS detector*, *JHEP* **02** (2024) 128 [[2311.03944](#)].
- [26] ATLAS collaboration, *Search for new resonances in mass distributions of jet pairs using 139 fb^{-1} of pp collisions at $\sqrt{s} = 13$ TeV with the ATLAS detector*, *JHEP* **03** (2020) 145 [[1910.08447](#)].
- [27] CMS collaboration, *Dark sector searches with the CMS experiment*, [2405.13778](#).
- [28] CMS collaboration, *Search for dijet resonances using events with three jets in proton-proton collisions at $s=13\text{TeV}$* , *Phys. Lett. B* **805** (2020) 135448 [[1911.03761](#)].
- [29] ATLAS collaboration, *Search for low-mass resonances decaying into two jets and produced in association with a photon or a jet at $\sqrt{s} = 13$ TeV with the ATLAS detector*, [2403.08547](#).
- [30] J. Alwall, R. Frederix, S. Frixione, V. Hirschi, F. Maltoni, O. Mattelaer et al., *The automated computation of tree-level and next-to-leading order differential cross sections, and their matching to parton shower simulations*, *JHEP* **07** (2014) 079 [[1405.0301](#)].
- [31] T. Sjöstrand, S. Ask, J.R. Christiansen, R. Corke, N. Desai, P. Ilten et al., *An introduction to PYTHIA 8.2*, *Comput. Phys. Commun.* **191** (2015) 159 [[1410.3012](#)].
- [32] DELPHES 3 collaboration, *DELPHES 3, A modular framework for fast simulation of a generic collider experiment*, *JHEP* **02** (2014) 057 [[1307.6346](#)].
- [33] L. Lonnblad and S. Prestel, *Matching tree-level matrix elements with interleaved showers*, *JHEP* **03** (2012) 019 [[1109.4829](#)].
- [34] A. Albert et al., *Recommendations of the LHC dark matter working group: Comparing LHC searches for dark matter mediators in visible and invisible decay channels and calculations of the thermal relic density*, *Phys. Dark Univ.* **26** (2019) 100377 [[1703.05703](#)].

- [35] C.G. Lester and D.J. Summers, *Measuring masses of semiinvisibly decaying particles pair produced at hadron colliders*, *Phys. Lett. B* **463** (1999) 99 [[hep-ph/9906349](#)].
- [36] C.G. Lester and B. Nachman, *Bisection-based asymmetric M_{T2} computation: a higher precision calculator than existing symmetric methods*, *JHEP* **03** (2015) 100 [[1411.4312](#)].
- [37] H. Beauchesne and G. Grilli di Cortona, *Event-level variables for semivisible jets using anomalous jet tagging*, in *Snowmass 2021*, 11, 2021 [[2111.12156](#)].
- [38] K. Choi, J.S. Lee and C.B. Park, *Measuring the Higgs boson mass with transverse mass variables*, *Phys. Rev. D* **82** (2010) 113017.
- [39] K. Pedro and P. Shyamsundar, *Optimal mass variables for semivisible jets*, *SciPost Phys. Core* **6** (2023) 067 [[2303.16253](#)].
- [40] R. Ellis, I. Hinchliffe, M. Soldate and J. Van Der Bij, *Higgs decay to $\tau^+\tau^-$ —A possible signature of intermediate mass Higgs bosons at high energy hadron colliders*, *Nucl. Phys. B* **297** (1988) 221.
- [41] M. Cacciari, G.P. Salam and G. Soyez, *The anti- k_T jet clustering algorithm*, *JHEP* **04** (2008) 063 [[0802.1189](#)].
- [42] M. Cacciari, G.P. Salam and G. Soyez, *FastJet user manual*, *Eur. Phys. J. C* **72** (2012) 1896 [[1111.6097](#)].
- [43] M. Dasgupta, A. Fregoso, S. Marzani and G.P. Salam, *Towards an understanding of jet substructure*, *JHEP* **09** (2013) 029 [[1307.0007](#)].
- [44] G. Cowan, K. Cranmer, E. Gross and O. Vitells, *Asymptotic formulae for likelihood-based tests of new physics*, *Eur. Phys. J. C* **71** (2011) 1554 [[1007.1727](#)].
- [45] L. Heinrich, M. Feickert and G. Stark, “pyhf: v0.7.6.” 10.5281/zenodo.1169739.
- [46] L. Heinrich, M. Feickert, G. Stark and K. Cranmer, *pyhf: pure-python implementation of histfactory statistical models*, *J. Open Source Softw.* **6** (2021) 2823.
- [47] T. Cohen, J. Roloff and C. Scherb, *Dark sector showers in the Lund jet plane*, *Phys. Rev. D* **108** (2023) L031501 [[2301.07732](#)].
- [48] E. Bernreuther, T. Finke, F. Kahlhoefer, M. Krämer and A. Mück, *Casting a graph net to catch dark showers*, *SciPost Phys.* **10** (2021) 046 [[2006.08639](#)].
- [49] F. Canelli, A. de Cosa, L.L. Pottier, J. Niedziela, K. Pedro and M. Pierini, *Autoencoders for semivisible jet detection*, *JHEP* **02** (2022) 074 [[2112.02864](#)].
- [50] D. Kar and S. Sinha, *Exploring jet substructure in semi-visible jets*, *SciPost Phys.* **10** (2021) 084.
- [51] T. Faucett, S.-C. Hsu and D. Whiteson, *Learning to identify semi-visible jets*, *JHEP* **12** (2022) 132 [[2208.10062](#)].
- [52] M. Park and M. Zhang, *Tagging a jet from a dark sector with Jet-substructures at colliders*, *Phys. Rev. D* **100** (2019) 115009 [[1712.09279](#)].